

Controllable Urchin-Like NiCo₂S₄ Microsphere Synergized with Sulfur-Doped Graphene as Bifunctional Catalyst for Superior Rechargeable Zn–Air Battery

Wenwen Liu, Jing Zhang, Zhengyu Bai,* Gaopeng Jiang, Matthew Li, Kun Feng, Lin Yang, Yuanli Ding, Tongwen Yu, Zhongwei Chen,* and Aiping Yu*

Rechargeable zinc–air batteries (ZnABs) are attracting great interest due to their high theoretical specific energy, safety, and economic viability. However, their performance and large-scale practical applications are largely limited by poor durability and high overpotential on the air-cathode due to the slow kinetics of the oxygen reduction and evolution reactions (ORR/OER). Therefore, it is highly desired to exploit an ideal bifunctional catalyst to endow the obtained ZnABs with excellent ORR/OER catalytic performances. Herein, a new nonprecious-metal bifunctional catalyst of urchin-like NiCo₂S₄ microsphere synergized with sulfur-doped graphene nanosheets (S-GNS/NiCo₂S₄) is controllably designed and synthesized by simply tailoring the structure and electronic arrangement, which endow the as-prepared catalyst with excellent electroactivity and long-term durability toward ORR and OER. Importantly, ZnABs constructed by this outstanding catalyst exhibit high power density, small charge/discharge voltage gap, and excellent cycle stability, notably outperforming the more costly commercial Pt/C + Ir/C mixture catalyst. These excellent electrocatalytic performances together with the simplicity of the synthetic method, make the urchin-like NiCo₂S₄ microsphere/S-GNS hybrid nanostructure exhibit great promise as a superior air-cathode catalyst for high-performance rechargeable ZnABs.

batteries' (ZnABs) possesses higher energy density (1086 Wh kg⁻¹), better safety, lower cost, and more environmental benignity,^[10–12] rendering it an extremely promising candidate system. However, their performances and large-scale applications are widely impeded by their limitations in rechargeability, power density, and energy efficiency.^[13] All of these drawbacks are mainly from the fundamental challenge of air-cathode with the slow kinetics of oxygen reduction and evolution (ORR/OER) reactions as well as poor durability.^[14,15] As one core components of the air-cathode, bifunctional catalysts simultaneously accelerating the ORR and OER, mainly contribute to the electrochemical performance of the air-cathode, and thus determine the performance of ZnABs. Up to now, Pt/C is commonly recognized as highly efficient ORR catalyst and Ir/C exhibits promising potential in OER.^[16] However, the widespread utilization of Pt/C and Ir/C is limited by their high cost, scarcity, and poor durability.^[16–18] In this

case, developing of highly efficient bifunctional catalysts with low-cost and high durability have become the top priority for boosting the air-electrode electrochemical reactions, and finally enhancing the overall performance of ZnABs.

Currently, transition metal chalcogenides (TMCs), as a new family of nonprecious electrocatalysts, have drawn the attentions of researchers due to its unique physicochemical properties, low cost, and environmental compatibility.^[19,20] Among these TMCs, ternary sulfides have gained rather extensive attention in the field of supercapacitors, batteries, and fuel cells originating from their outstanding electrochemical

1. Introduction

In response to the challenging of energy crisis, global warming, and environment pollution, the immediate imperative is to develop novel, green, high-performance energy storage, and conversion systems instead of using conventional fossil fuel based energy systems.^[1,2] Among these energy storage and conversion systems, batteries, as one of the most efficient and promising systems to address the abovementioned problems, have attracted tremendous interest because of their unique advantages.^[3–9] Compared with other battery systems, Zn–air

W. Liu, J. Zhang, G. Jiang, M. Li, K. Feng, Dr. Y. Ding, Dr. T. Yu, Prof. Z. Chen, Prof. A. Yu
Department of Chemical Engineering
Waterloo Institute for Nanotechnology
University of Waterloo
Waterloo, Ontario N2L3G1, Canada
E-mail: zhwenchen@uwaterloo.ca; aipingyu@uwaterloo.ca

W. Liu, Prof. Z. Bai, Prof. L. Yang
School of Chemistry and Chemical Engineering
Key Laboratory of Green Chemical Media and Reaction
Ministry of Education
Collaborative Innovation Center of Henan Province
for Fine Chemicals Green Manufacturing
Henan Normal University
Xinxiang 453007, China
E-mail: baizhengyu2000@163.com

 The ORCID identification number(s) for the author(s) of this article can be found under <https://doi.org/10.1002/adfm.201706675>.

DOI: 10.1002/adfm.201706675

performance.^[21,22] In particular, NiCo₂S₄, as one of the most famous ternary sulfides, has received considerable interest to the scientific community owing to its relative high electrical conductivity, multiple valences and abundant crystallographic structures endowing it with high electrochemical activity.^[23,24] Although recent efforts have been made to investigate the ORR or/and OER activities of NiCo₂S₄,^[25,26] unsatisfactory performances still exist such as the limited catalytic activity arising from the sluggish ion/electron transport kinetic of NiCo₂S₄ and the undesirable cycle stability due to its structural change coupled with the complicated preparation procedures,^[27,28] thus hinder its large-scale applications in ZnABs. Therefore, the huge challenge presented here is how to elaborately design, controllably synthesize and rationally assemble to build an efficient and robust NiCo₂S₄-based bifunctional catalyst with highly activity and excellent durability for ZnABs.

As reported, the catalytic behaviors of bifunctional catalysts could be dramatically enhanced by nanostructured strategies through the optimization of morphological architecture, surface configuration, and electronic state.^[28,29] Furthermore, recent studies have shown that the electrochemical performances of nonprecious electrocatalysts can be improved by combining with heteroatom doped carbon materials,^[30–32] which endow the obtained electrocatalysts with high activity and excellent durability by improving electron conductivity, enhancing structural stability, and providing more efficient ion contact angle between electrolyte and electrode. Compared with other carbon materials, sulfur-doped graphene nanosheet (S-GNS) possess unique structure and physicochemical properties owing to the effective modulation of the electronic properties of graphene by chemical substitutional doping,^[32,33] making S-GNS an ideal matrix to construct the novel high-performance bifunctional catalysts. According to the discussion above, it inspires us to think whether it is possible to enhance the ORR and OER performances of NiCo₂S₄ using nanostructured strategies through rational morphology design, precise composition control, and the combination of S-GNS.

Based on the above-mentioned considerations, urchin-like NiCo₂S₄ microsphere wrapped by S-GNS has been controllably designed and prepared by adjusting the parameter of hydrothermal reaction and subsequent sulfurization process in this work. Encouragingly, the as-prepared S-GNS/NiCo₂S₄ hybrid catalyst exhibits superior electrocatalytic activities toward ORR and OER in alkaline electrolyte. Most importantly, the constructed rechargeable ZnABs with S-GNS/NiCo₂S₄ catalyst show a maximum power density of 216.3 mW cm⁻², a small overpotential (1.09 V), and excellent stability without obvious decay after 100 h. The high electrocatalytic activities of S-GNS/NiCo₂S₄ catalyst for OER and ORR are attributed to its unique morphology and structure and the synergistic effect between urchin-like NiCo₂S₄ microsphere and S-GNS. First, urchin-like NiCo₂S₄ is well assembled by nanoneedles with microspherical architecture, which drastically enhances the surface exposure of active sites endowing such morphology with efficient mass and charge transport pathways. Apart from increasing the electrical conductivity, S-GNS can also improve the contact between catalyst and electrolyte, and maintain the integration of the catalyst during charge/discharge process due to the robust nature of GNS, thus leading to improved cycling stability. Additionally,

S-GNS also enhances electrocatalytic activity, which is attributed to the sulfur-doping causing the change in the spin density of carbon atom adjacent to the heteroatom.

2. Results and Discussion

2.1. Physicochemical Characterizations

To elucidate the growth mechanism of urchin-like NiCo-based carbonate hydroxide microsphere (Figure S1, Supporting Information), their morphologies synthesized under different reaction times were studied by scanning electron microscopy (SEM). As shown in Figure 1a–h, the morphologies of the synthesized urchin-like NiCo-based carbonate hydroxide microspheres are time dependent. Based on the morphology evolution, a possible growth process is put forward as shown in Figure 1i. In the initial reaction stage, many initial crystal nuclei have been formed by the reaction of metal cations (Co²⁺ and Ni²⁺) with carbonate and hydroxy anions produced by the hydrolysis of urea at high temperature.^[34,35] Due to the high thermodynamic instability of ultrahigh surface energy nanonuclei, these crystal nanonuclei will tend to aggregate together forming large secondary structures. Any additional NiCo-based carbonate material will grow onto the lattice of the aggregated nuclei. However, the primary crystal has a preferred growth orientation along the c-axis due to the different electronic structure of each metal ion. Co²⁺ tends to prefer an octahedral coordination, whereas Ni²⁺ tends to favor a square-planar coordination, which results in the formation of 1D nanoneedles self-assembled into a microsphere morphology.^[35] As the reaction progresses, these microspheres gradually transform into robust urchin-like microspheres. Additionally, NiCo-based carbonate hydroxide with different Ni/Co ratios have also been synthesized by adjusting the ratios of the starting materials (Figure S2, Supporting Information). The morphology variations and structure evolutions of these NiCo-based carbonate hydroxide microsphere after annealing (Figure S3, Supporting Information) and their corresponding composition- and structure-dependent electrocatalytic performance (Figure S4, Supporting Information) have been thoroughly investigated. As a result, the optimal NiCo-oxide with a Ni/Co ratio of 1:2 exhibits unique morphology and superior electrocatalytic performance, and thus is chosen as an intermediate product to further design and construct the final product of S-GNS/NiCo₂S₄.

The representative low-magnification SEM image (Figure 2a) shows that the obtained NiCo₂S₄ converted from NiCo₂O₄ (Figure S5, Supporting Information) has spherical morphology with relative uniform size. It can be observed that the urchin-like hierarchical micro/nanostructure is completely maintained after sulfidation process, suggesting excellent structural stability. High-magnification SEM image (Figure 2b) displays the individual microsphere of the NiCo₂S₄ with a diameter of about 3.1–5.9 μm with numerous nanoneedles radially protruded from the center. Importantly, there are many mesoporous among the nanoneedles (Figure 2c), which provide more effective active sites and ensure good electrolyte accessibility during the catalytic reaction. Figure 2d–f shows the representative SEM images of the synthesized S-GNS/NiCo₂S₄

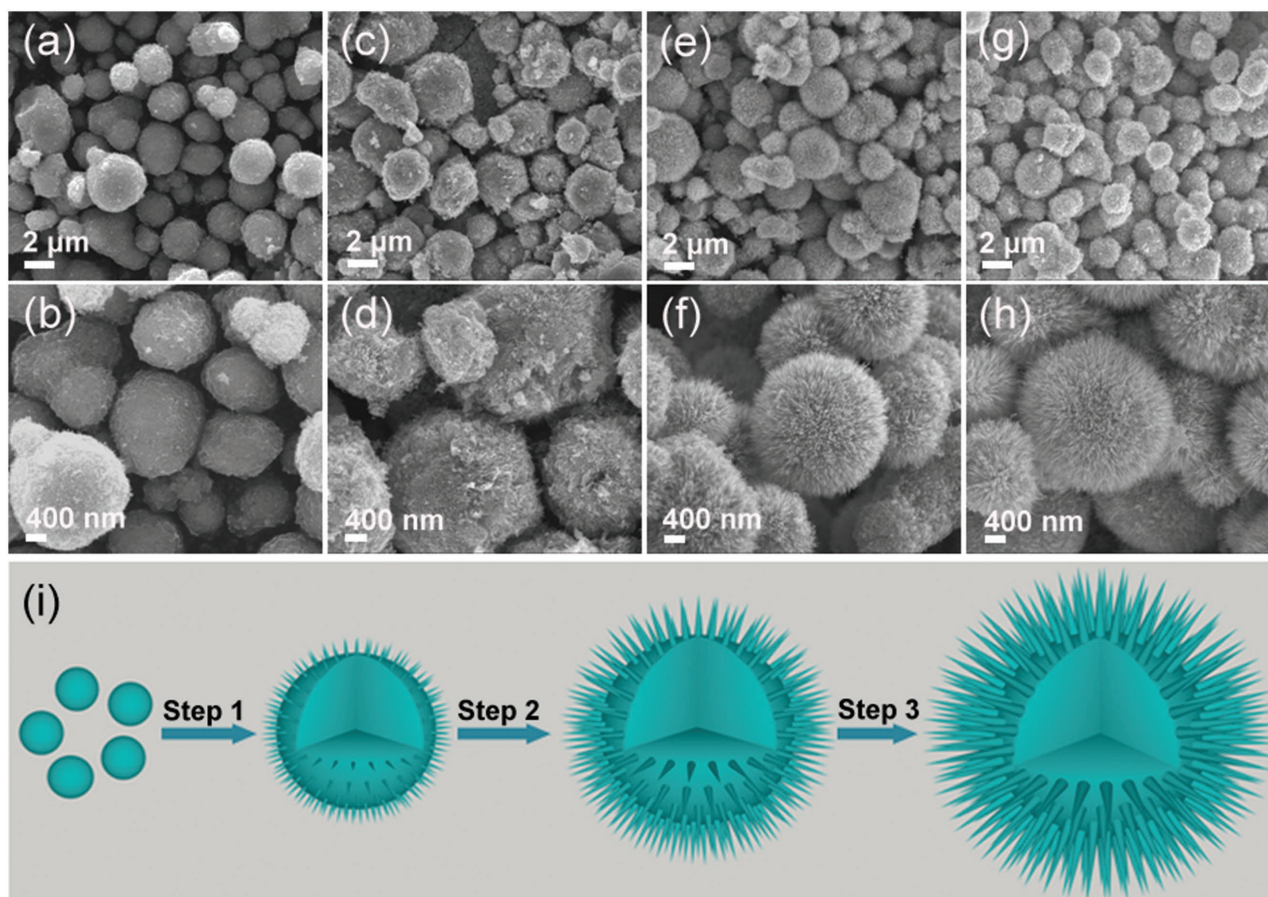


Figure 1. SEM images with different magnifications of the obtained NiCo-based carbonate hydroxide under different synthesis time: a,b) 1 h; c,d) 2 h; e,f) 4 h; and g,h) 8 h. i) Schematic diagram for the evaluation and formation process of urchin-like NiCo-based carbonate hydroxide microsphere.

composites with different magnifications. Evidently, the urchin-like NiCo_2S_4 microsphere is well encapsulated by the ultrathin S-GNS forming a porous 3D-interconnected network, which could effectively improve the conductivity of the catalyst, increase the electroactive region, shorten the ion diffusion pathway while preventing the collapse of urchin-like NiCo_2S_4 microsphere during the electrochemical process. Transmission electron microscopy (TEM) is carried out to characterize the detailed morphology and crystal structure of S-GNS/ NiCo_2S_4 . The typical low-magnification TEM image (Figure 3a) reveals that the urchin-like NiCo_2S_4 microspheres are well wrapped by the highly conductive ultrathin S-GNS, which could provide a direct electron transfer pathway, enhance the structure stability, and improve the catalytic activity. TEM image (Figure 3b) shows that the diameter of the urchin-like NiCo_2S_4 microsphere is in the range of 3.2–3.5 μm , and each individual urchin-like NiCo_2S_4 microsphere is composed of numerous primary nanoneedles with a width ranging from 10 to 40 nm and a length of ≈ 200 –250 nm (Figure 3c), corroborating the SEM images. The high-magnification TEM image (Figure 3d) confirms that each building block of the nanoneedle consists of connected small nanocrystals and possesses the porous structure which stems from the release of H_2O and CO_2 during the decomposition process^[36,37] This porous structure of urchin-like NiCo_2S_4 microsphere can be further

identified by its corresponding nitrogen adsorption–desorption isotherms and pore-size distribution discussed later. Furthermore, high-resolution TEM image (Figure 3e) indicates a lattice spacing of 0.28 and 0.54 nm corresponding, respectively, to the (311) and (111) planes of the NiCo_2S_4 crystal.^[38,39] The corresponding spectral analysis by fast Fourier transform pattern (Figure S6, Supporting Information) indicates the polycrystalline nature of NiCo_2S_4 .^[40] Elemental mappings (Figure 3f) verify the uniform distribution of Ni, Co, S, and C elements in the S-GNS/ NiCo_2S_4 sample. It is well-known that large surface area and high porosity are crucial for the catalysts with high activity. Therefore, the pore structure and surface area of the as-prepared NiCo_2S_4 and S-GNS/ NiCo_2S_4 are investigated by nitrogen adsorption–desorption isotherms. As shown in Figure S7a,c (Supporting Information), both samples show a type-IV isotherm with a remarkable hysteresis loop at relative high pressure, indicating their mesoporous characteristic nature. It is noted that the specific surface area for the S-GNS/ NiCo_2S_4 is calculated to be 227 $\text{m}^2 \text{g}^{-1}$, which is larger than that of NiCo_2S_4 (163 $\text{m}^2 \text{g}^{-1}$), demonstrating the NiCo_2S_4 synergized with sulfur-doped graphene can provide more active sites for redox reaction. In addition, compared with the pore size distribution of the urchin-like NiCo_2S_4 microsphere centered at 5.6 nm (Figure S7b, Supporting Information), whereas the S-GNS/ NiCo_2S_4 shows a broad pore size distribution in the wide range

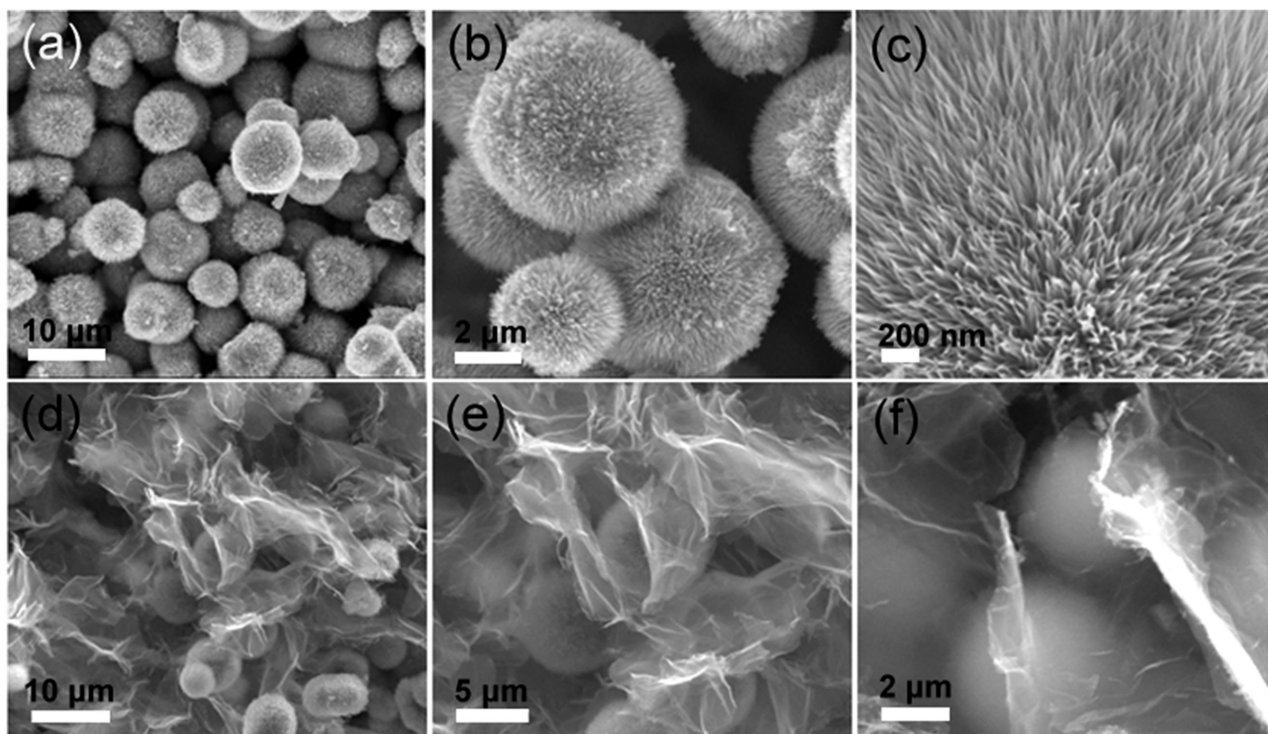


Figure 2. SEM images with different magnifications of a–c) the obtained urchin-like NiCo_2S_4 microsphere and d–f) S-GNS/ NiCo_2S_4 composites.

of 1–325 nm with two major pore size distributions centered at around 9.8 and 52.8 nm (Figure S7d, Supporting Information), respectively. The high brunauer–emmett–teller (BET) specific surface and the broad pore distribution can provide effective

triple phase regions required for reactions and offer the efficient transport of electrons and ions, thus beneficial for the electrocatalytic performances. Besides, the electrochemical active surface area, which is closely related to the catalytic activity and is

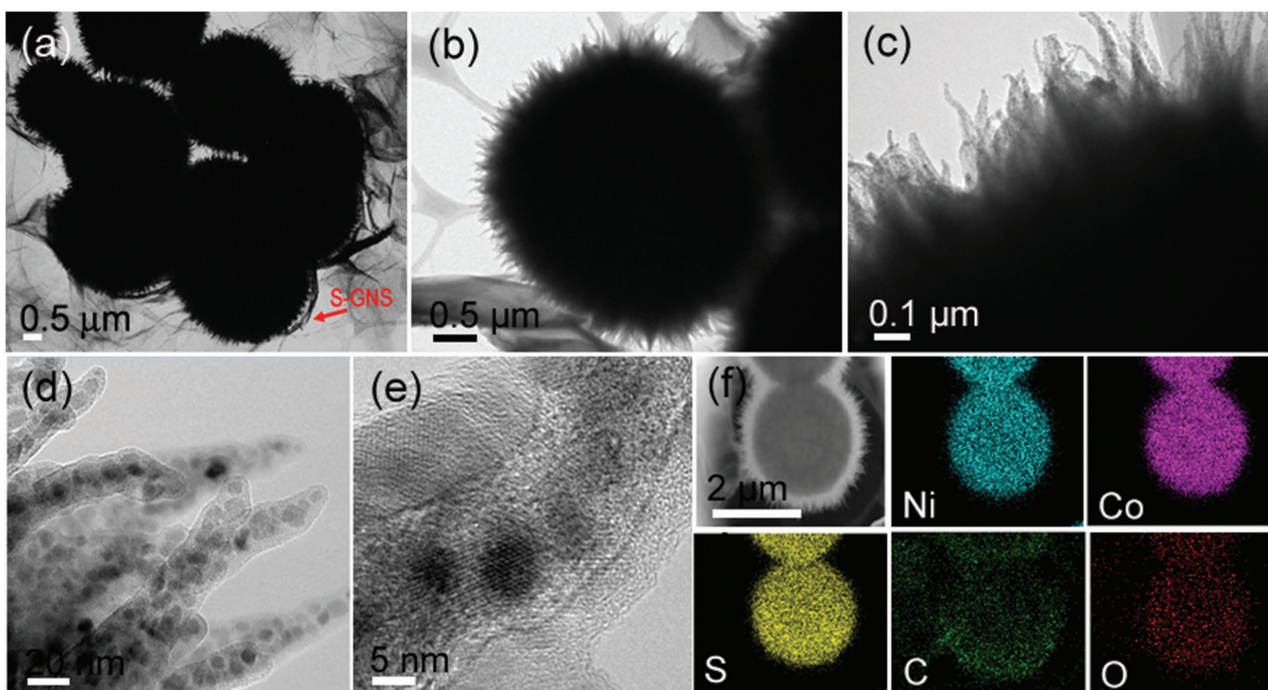


Figure 3. a,b) Low-magnification TEM images; c,d) high-magnification TEM images; e) high-resolution TEM image; and f) element mappings of nickel, cobalt, sulfur, carbon, and oxygen in the as-obtained S-GNS/ NiCo_2S_4 nanocomposite.

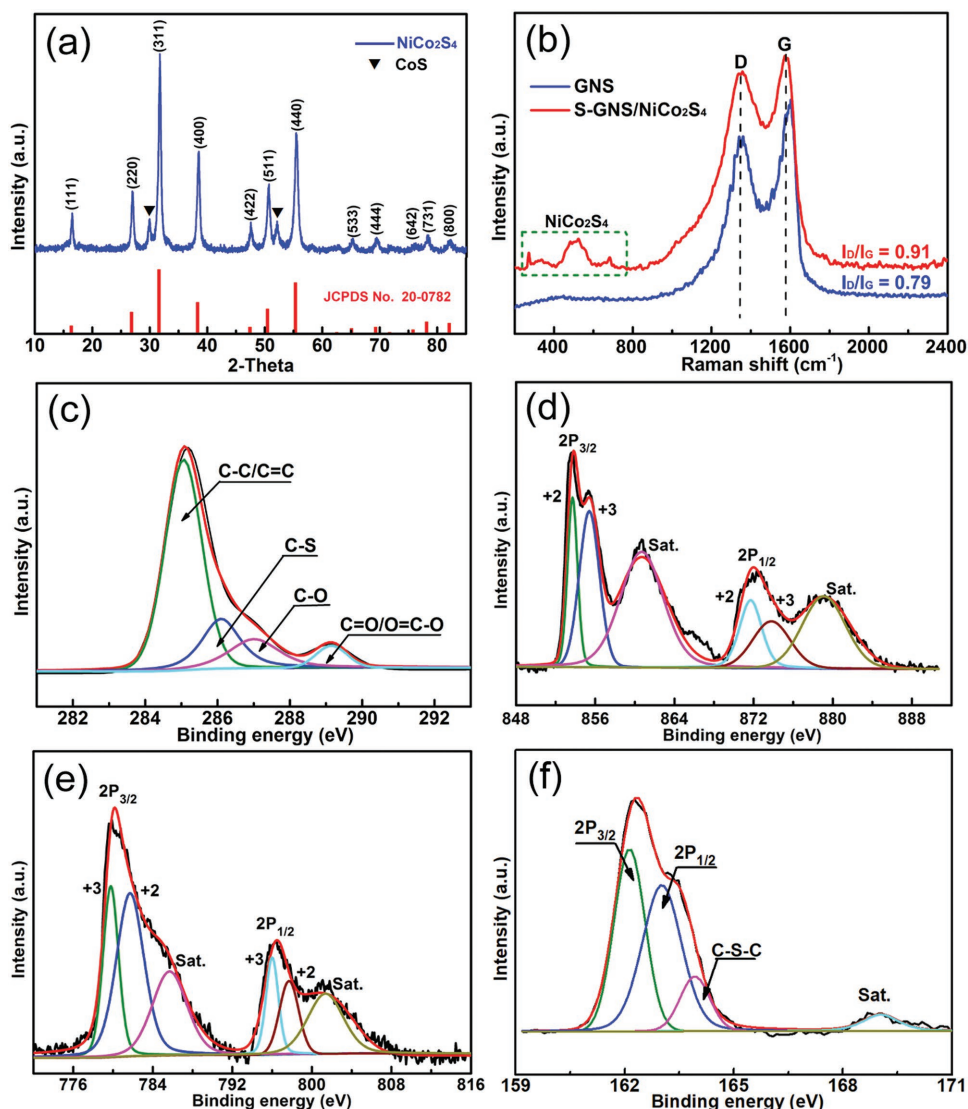


Figure 4. a) XRD spectrum and b) Raman spectrum of the as-prepared S-GNS/NiCo₂S₄ nanocomposite; XPS spectrum of the S-GNS/NiCo₂S₄ composite: c) C 1s, d) Ni 2p, e) Co 2p, and f) S 2p, respectively.

evaluated by the double-layer capacitance (C_{dl}) determined via cyclic voltammetry (CV) measurements at different scan rates (Figure S8, Supporting Information). The C_{dl} (14.1 mF cm⁻²) of S-GNS/NiCo₂S₄ is larger than that of NiCo₂S₄ (7.9 mF cm⁻²), indicating more exposed active sites for ORR and OER owing to the larger specific surface area and hierarchical porous structure of S-GNS/urchin-like NiCo₂S₄ microsphere.

The crystalline phase of the as-prepared S-GNS/NiCo₂S₄ is revealed by the X-ray diffraction (XRD) spectrum (Figure 4a). All the diffraction peaks at 16.3°, 26.8°, 31.5°, 38.1°, 47.5°, 50.4°, 55.2°, 65.1°, 69.3°, 75.8°, 78.2°, and 82.1° correspond to the (111), (220), (311), (400), (422), (511), (440), (533), (444), (642), (731), and (800) planes of the nanostructured cubic type NiCo₂S₄ (JCPDS Card no. 20-0782), in exception to two small peaks at 29.8° and 52.2° attributed to the CoS,^[41,42] suggesting successful conversion of NiCo₂O₄ into NiCo₂S₄ via sulfuration process. It should be mentioned that no diffraction peak from S-GNS is observed due to overlapping of the main peak

of S-GNS with low intensity at 26.3° and the (220) peak of cubic type NiCo₂S₄ with high intensity at 26.8°. Moreover, compared with the Raman spectrum of the GNS (Figure 4b), the Raman spectrum of the S-GNS/NiCo₂S₄ not only exhibits the characteristic peaks around 332.1, 524.3, and 677.7 cm⁻¹, attributed to the T_{2g}, F_{2g}, and A_{1g} stretching modes of NiCo₂S₄,^[43] respectively, but also shows an increase of the I_D/I_G ratio (from 0.79 to 0.91), which reveals that sulfur-doping causes some structural distortion in GNS because a larger I_D/I_G ratio means more defects and distortions. Additionally, the G peak of the S-GNS/NiCo₂S₄ sample shows an obvious redshift compared to that of the pristine GNS, which is an important characteristic of n-type substitutional doping of GNS.^[44] Raman spectroscopy strongly confirms the sulfur bonding with carbon with n-type doping.

To reveal the elemental composition and chemical state in the S-GNS/NiCo₂S₄ nanostructure, X-ray photoelectron spectroscopy (XPS) measurements are carried out and the corresponding results are displayed in Figure 4c–f. By using

a Gaussian fitting, the C 1s spectrum (Figure 4c) not only shows relative lower peak intensities of the C–C, C=O, and O–C–O peaks compared with those of the graphene oxide (GO) (Figure S9, Supporting Information), but also has an obvious C–S peak located at 286.4 eV, indicating the removal of a large number of oxygen functional groups and the successful incorporation of S into the GNS by creating C–S covalent bonds.^[45] As reported, the doping of sulfur depends more on the available substitutional and defect sites.^[44,46] Therefore, we believe the covalent C–S bonds are formed through the reaction between GO's oxygen containing functional groups (e.g., carbonyl, carboxyl, and carboxylate groups) and S. This occurs because more vacancies are generated during the sulfuration process due to the loss of oxygenated species,^[44] which can provide more opportunity for sulfur atom to bond with the carbon host. The C 1s spectrum confirms that S atoms have been successfully incorporated into the GNS framework via covalent bonds, which agrees well with the result of Raman spectrum.

Furthermore, the energies at around 854.7 and 872.4 eV (Figure 4d) are attributed to Ni 2p_{3/2} and Ni 2p_{1/2}, respectively, demonstrating the existence of both Ni²⁺ and Ni³⁺ in the S-GNS/NiCo₂S₄ sample,^[39,47] but the strong satellite peaks indicate that Ni²⁺ represents a significant proportional of the Ni in the sample. The binding energies at 780.2 and 796.5 eV (Figure 4e) correspond to Co 2p_{3/2} and Co 2p_{1/2}, confirms the presence of both Co³⁺ and Co²⁺ in the sample,^[39,47] while the weak satellite peaks reveal that the majority of cobalt element is in Co³⁺ oxidation state. Figure 4f shows the spectrum of the S2p, where the binding energies at around 161.8 and 163.2 eV are assigned to S2p_{3/2} and S2p_{1/2}, respectively, corresponding to metal-sulfur (M–S) bond in the NiCo₂S₄.^[39,47] The peak at around 164.3 eV can be ascribed to C–S–C bond,^[48] indicating that sulfur atoms are bonded to carbon atoms in graphene matrix. Furthermore, the binding energy at 169.1 eV is assigned to the sulfur atom at low coordination near the surface.^[39,47] Results from XRD, Raman, and XPS demonstrates that our designed S-GNS wrapped urchin-like NiCo₂S₄ microsphere has been successfully prepared.

2.2. Electrochemical Characterizations

CV technique is first carried out to investigate the ORR catalytic activities of the as-prepared NiCo₂O₄, NiCo₂S₄, and S-GNS/NiCo₂S₄ materials in a standard three-electrode system. A characteristic cathodic peak is observed in the CV curves of NiCo₂O₄, NiCo₂S₄, and S-GNS/NiCo₂S₄ materials in O₂-saturated 0.1 M KOH electrolyte (Figure 5a), but it does not appear in their corresponding CV curves in N₂-saturated 0.1 M KOH electrolyte, revealing the ORR catalytic activities of NiCo₂O₄, NiCo₂S₄, and S-GNS/NiCo₂S₄ nanocomposite.^[26,28] Especially, the cathodic peak potential of S-GNS/NiCo₂S₄ locate at 0.85 V, which is more positive than those of NiCo₂O₄ (0.64 V) and NiCo₂S₄ (0.70 V), and comparable to that of commercial Pt/C catalyst (0.89 V). This result indicates that the S-GNS/NiCo₂S₄ catalyst has the best ORR catalytic activity among these prepared three catalysts, which can be further confirmed by the results determined from the linear scan voltammeter (LSV) curves. As shown in Figure 5b, the S-GNS/NiCo₂S₄ catalyst

exhibit the lowest overpotential, highest half-wave potential ($E_{1/2}$) and largest reduction current compared to those of NiCo₂S₄ and NiCo₂O₄ catalysts. Encouragingly, the current densities of S-GNS/NiCo₂S₄ catalyst between 0.10 and 0.53 V are even larger than those of commercial Pt/C catalyst, and the $E_{1/2}$ of S-GNS/NiCo₂S₄ (0.88 V) is only about 10 mV more negative than that of commercial Pt/C catalyst (0.89 V), indicating the excellent electrocatalytic activity of the S-GNS/NiCo₂S₄ catalyst. The enhanced electrocatalytic activity of S-GNS/NiCo₂S₄ catalyst toward ORR can be attributed to the urchin-like NiCo₂S₄ microsphere with the unique hierarchical structure assembled from mesoporous nanoneedles, and the synergistic benefits from the rational integration of urchin-like NiCo₂S₄ microsphere into S-GNS. In a word, this unique architecture can facilitate the exposure of more catalytic active sites and provide the efficient transport pathways for reactant species, endowing S-GNS/NiCo₂S₄ catalyst with a promising catalytic performance for ORR.

LSV curves at different rotation speeds (Figure 5c) are used to investigate the electron transfer kinetic of the ORR process for the S-GNS/NiCo₂S₄. When the rotation speeds were ramped from 400 to 2400 rpm, the current densities increased accordingly which is due to the enhanced convectional mass transfer of oxygen molecule from the bulk electrolyte to the electrode surface. Most importantly, the Koutecky–Levich (K–L) plots of the S-GNS/NiCo₂S₄ catalyst exhibit good linearity and parallelism at various potentials (Figure 5d), indicating that the reaction rate is first-order with respect to the dissolved oxygen concentration.^[49,50] Meanwhile, the electron transfer number (*n*) derived from the slopes of the K–L plots is in the range of 3.86–3.96, demonstrating a direct four-electron transfer process of the S-GNS/NiCo₂S₄ catalyst toward the ORR. Besides the catalytic activities, the durability is also a very important parameter for the application of catalyst. The durability of S-GNS/NiCo₂S₄ nanomaterial is evaluated by chronoamperometric measurement at 0.65 V in O₂-saturated 0.1 M KOH (Figure S10, Supporting Information). The relative current of the S-GNS/NiCo₂S₄ nanocomposite is still 90.9% after 10 h, while the value is only 70.2% for commercial Pt/C catalyst, indicating the superior durability of the S-GNS/NiCo₂S₄ nanocomposite over commercial Pt/C. Therefore, the S-GNS/NiCo₂S₄ nanomaterial is highly promising as superior ORR catalyst owing to its high catalytic activity and excellent electrochemical stability.

An efficient bifunctional catalyst used as the cathode of ZnABs should not only possess the outstanding ORR catalytic activity and durability but also the excellent OER catalytic activity. The OER catalytic activity of S-GNS/NiCo₂S₄ nanomaterial is evidenced by the LSV curves (Figure 5e). It can be observed that the OER potential of S-GNS/NiCo₂S₄ at 10 mA cm⁻² is only 1.56 V, which is smaller than that of NiCo₂O₄ (1.62 V) and NiCo₂S₄ (1.59 V), indicating the smallest overpotential of S-GNS/NiCo₂S₄ composite among the obtained three catalysts. Particularly, the overpotential of the S-GNS/NiCo₂S₄ (0.33 V) at 10 mA cm⁻² is even smaller than that of commercial Ir/C catalyst (0.45 V), demonstrating its superior electrocatalytic activity toward OER. Furthermore, S-GNS/NiCo₂S₄ composite exhibit the largest OER current density in the whole potential window among these four catalysts, also revealing the outstanding catalytic activity of S-GNS/NiCo₂S₄ nanocomposite

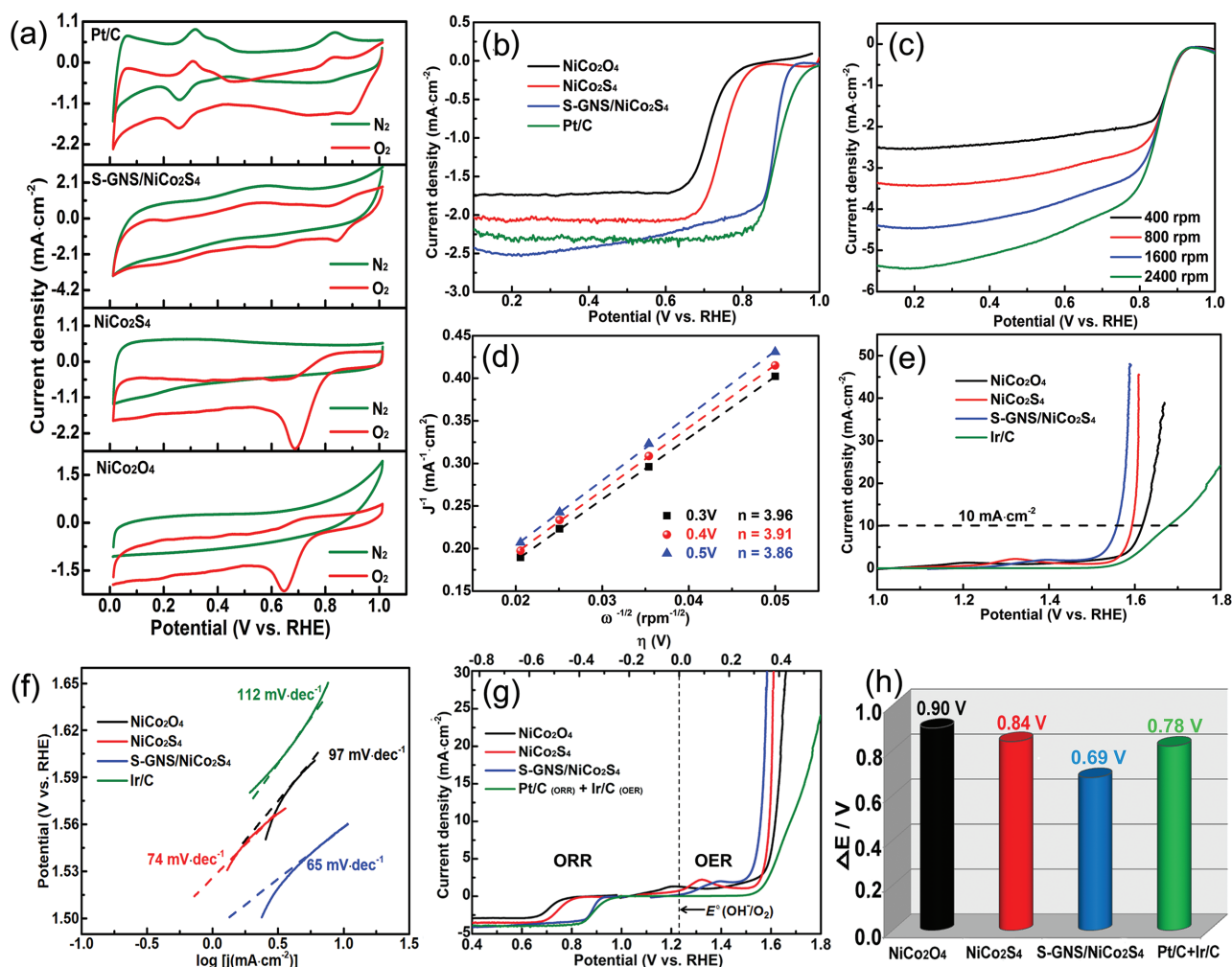


Figure 5. Electrocatalytic ORR activities of NiCo₂O₄, NiCo₂S₄, S-GNS/NiCo₂S₄, and Pt/C catalysts in a O₂-saturated 0.1 M KOH electrolyte: a) CV curves at 50 mV s⁻¹, b) LSV curves with the rotating speed of 400 rpm at 5 mV s⁻¹; c) LSV curves of the S-GNS/NiCo₂S₄ catalyst under various rotating speeds; d) K-L plots of the S-GNS/NiCo₂S₄ catalyst based on the obtained LSV curves; Electrocatalytic OER activities of NiCo₂O₄, NiCo₂S₄, S-GNS/NiCo₂S₄, and Pt/C catalysts in N₂-saturated 0.1 M KOH with the rotating speed of 1600 rpm at 5 mV s⁻¹: e) LSV curves; f) Tafel plots obtained from the corresponding LSV curves; g) ORR and OER curves of NiCo₂O₄, NiCo₂S₄, S-GNS/NiCo₂S₄, and Pt/C catalysts in O₂/N₂-saturated 0.1 M KOH electrolyte; h) Value of ΔE for NiCo₂O₄, NiCo₂S₄, S-GNS/NiCo₂S₄, Pt/C catalysts ($\Delta E = E_{10} - E_{1/2}$), respectively.

toward OER. In addition, the superior OER performance of S-GNS/NiCo₂S₄ nanocomposite is further supported by its small Tafel slope (65 mV dec⁻¹) (Figure 5f) compared with that of NiCo₂S₄ (74 mV dec⁻¹), NiCo₂O₄ (97 mV dec⁻¹), and commercial Ir/C (112 mV dec⁻¹). The chronoamperometric test (Figure S11, Supporting Information) reveals that the S-GNS/NiCo₂S₄ catalyst has a high stability with only 14.8% current decay after 10 h, whereas Ir/C displays a 29.7% current decay under the same condition.

Additionally, the potential difference ΔE ($\Delta E = E_{\text{OER}} - E_{\text{ORR}}$) between the potential under the OER current density of 10 mA cm⁻² and the half-wave potential of ORR is used to evaluate to the overall activity of bifunctional catalyst (Figure 5g). As reported, the smaller the ΔE value, the better is the catalytic activity of the bifunctional catalyst.^[51] As shown in Figure 5h, the ΔE value of the S-GNS/NiCo₂S₄ nanocomposite is only 0.69 V, smaller than that of Pt/C + Ir/C mixture catalyst (0.78 V), indicating a higher bifunctional activity of the S-GNS/NiCo₂S₄

nanocomposite toward ORR and OER. It is also found that the potential difference presented here is smaller or comparable to other high-performance bifunctional materials reported (Table S1, Supporting Information), further confirming the high bifunctional activity.

Based on the above outstanding ORR/OER catalytic activity and durability of S-GNS/NiCo₂S₄ nanocomposite, a home-made rechargeable ZnABs (Figure 6a) is constructed using S-GNS/NiCo₂S₄ nanocomposite as the catalyst of air-cathode to further demonstrate its practical application potential. All air-cathode electrodes are assembled in the same technique condition to ensure the comparability and reliability. As shown in Figure 6b, the maximum power density of the ZnABs based on the S-GNS/NiCo₂S₄ nanocomposite air-cathode is 216.3 mW cm⁻² at 0.67 V, which is higher than that of commercial Pt/C + Ir/C mixture catalyst (188.6 mW cm⁻² at 0.53 V) and those of other reported catalysts.^[52–55] These results indicate that ZnABs performance (peak power density and discharge polarization

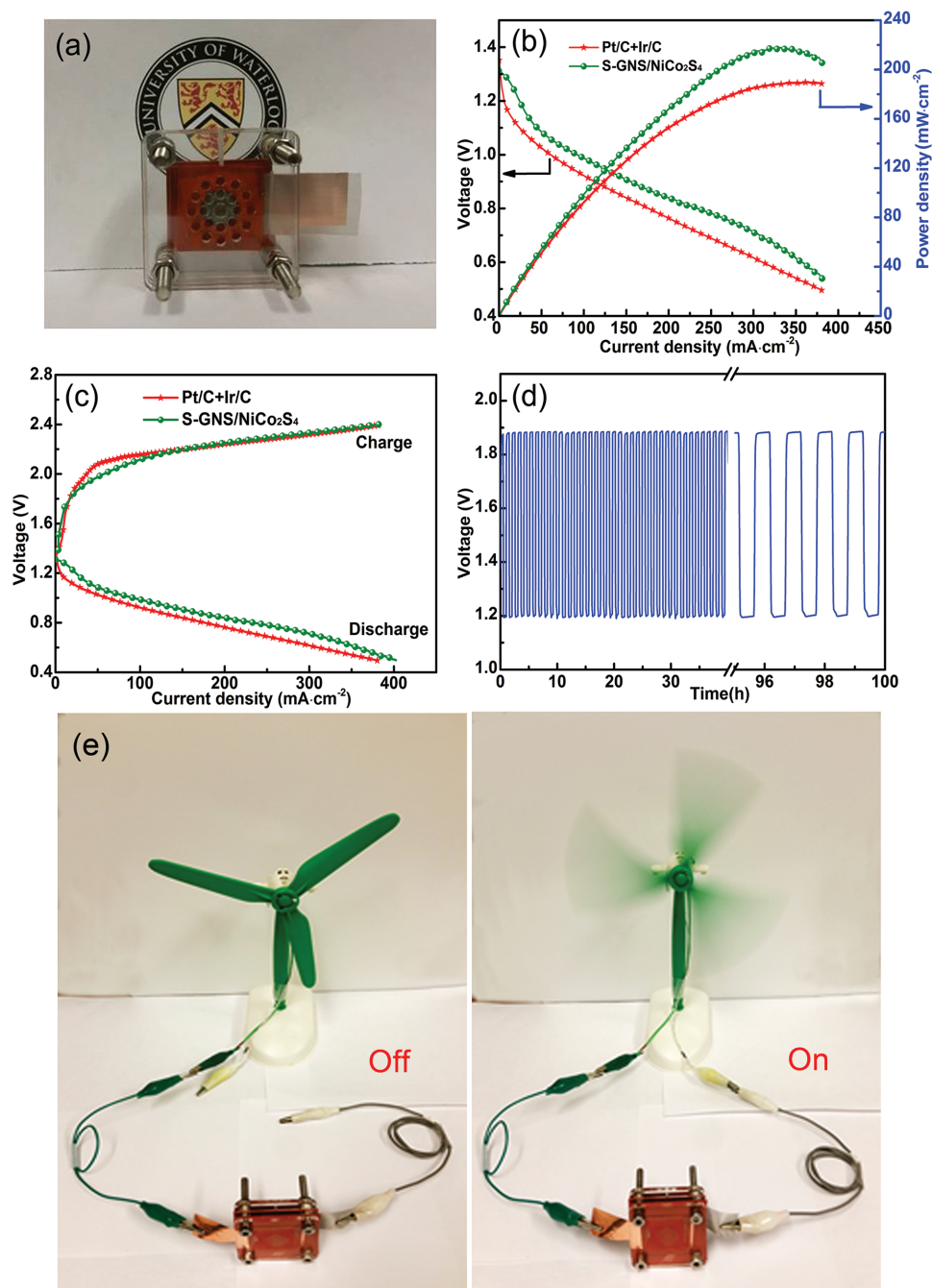


Figure 6. a) Photography of a home-made rechargeable ZnABs; b) Discharge polarization curves and their corresponding power density curves of the home-made rechargeable ZnABs based on the Pt/C + Ir/C mixture catalyst and S-GNS/NiCo₂S₄ catalyst, respectively; c) Charge/discharge polarization curves of the as-prepared ZnABs based on the Pt/C + Ir/C mixture catalyst and S-GNS/NiCo₂S₄ catalyst, respectively; d) Galvanostatic charge/discharge test of the home-made ZnABs built with S-GNS/NiCo₂S₄ catalyst at 10 mA cm⁻²; e) A home-made rechargeable ZnABs used to power a mini-fan.

voltage) has been significantly enhanced by the air-cathode based on the S-GNS/NiCo₂S₄ catalyst. Furthermore, the charge/discharge polarization curves (Figure 6c) show that the ZnABs based on S-GNS/NiCo₂S₄ catalyst possesses smaller charge/discharge polarization voltages compared to those of Pt/C + Ir/C mixture catalyst. These results further confirm that the S-GNS/NiCo₂S₄ nanocomposite outperform commercial Pt/C + Ir/C mixture catalyst by superior ORR and OER catalytic activities,

which corroborate well with the above other electrochemical results. The cycle stability of the ZnABs based on the S-GNS/NiCo₂S₄ nanocomposite is evaluated by galvanostatic technique shown in Figure 6d. It is noted that the initial discharge voltage plateau is at 1.19 V with the corresponding charging voltage plateau at 1.89 V at a high current density of 10 mA cm⁻² (40 min per cycle), which represents only a 0.80 V voltage difference between the charge and discharge process. Importantly,

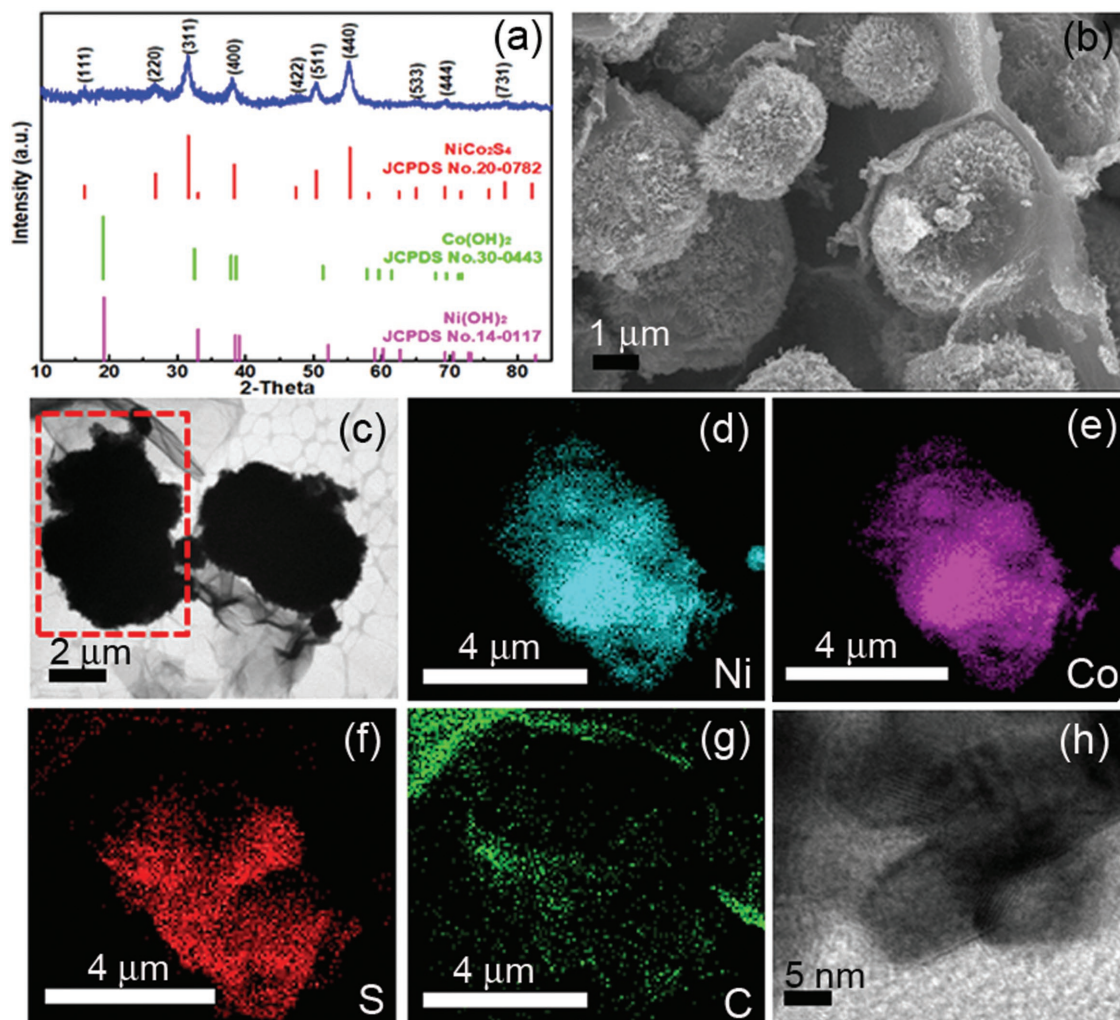


Figure 7. Morphology and composition characterization of S-GNS/NiCo₂S₄ after the stability test: a) XRD; b) SEM image; c) TEM image; Element mapping of d) nickel, e) cobalt, f) sulfur, and g) carbon; and h) High-resolution TEM (HRTEM) image.

no visible change of the charge and discharge voltage plateaus is observed even after 100 h continuous cycle, indicating excellent charge/discharge cycle stability of the ZnABs based on the S-GNS/NiCo₂S₄ nanocomposite. Excitingly, a home-made ZnABs can effectively power a mini-fan (Figure 6e), indicating its practical application to drive some electronic devices.

To gain insight into the deep reason behind the superior cycle stability, the morphology and composition of S-GNS/NiCo₂S₄ after the cycling test are evaluated by comprehensive XRD, SEM, and TEM characterizations. As shown in Figure 7a, all the diffraction peaks are attributed to the cubic type NiCo₂S₄ (JCPDS No. 20-0782), and no additional diffraction peaks corresponding to Co(OH)₂ and Ni(OH)₂ are detected, indicating minimal dissolution of NiCo₂S₄ in alkaline media during the ORR/OER processes. In addition, the S-GNS/NiCo₂S₄ catalyst still shows hierarchical morphology with the basic structure of urchin-like NiCo₂S₄ microsphere well preserved after the cycling test, demonstrating high mechanical strength and good structure stability of S-GNS/NiCo₂S₄ in the alkaline media (Figure 7b). Furthermore, the more detailed information of

structural and morphological features of the S-GNS/NiCo₂S₄ after the cycling test are characterized by TEM. It is noted from the TEM observations (Figure 7c) that the urchin-like NiCo₂S₄ microspheres maintain their structure integrity without obvious collapse after the cycling test, and still anchor onto the S-GNS. The corresponding element mappings (Figure 7d–g) and high-resolution TEM image (Figure 7h) also demonstrate that the electrode has its chemical composition almost unchanged after long-term cycling. Based on these observations, we can reasonably conclude that the superior durability of the S-GNS/NiCo₂S₄ bifunctional catalyst for Zn–air battery is due to the synergistic effect between S-GNS and NiCo₂S₄. Especially, the surface S-GNS layer effectively hinders the degradation of the S-GNS/NiCo₂S₄ electrode. It could not only act as an effective buffer layer to suppress the structural collapse of urchin-like NiCo₂S₄ microsphere, but also serve as a chemical blocking layer to slow down the change of chemical composition of the NiCo₂S₄ during cycling test.

The excellent electrochemical performance of S-GNS/NiCo₂S₄ nanocomposite served as the catalyst of air-cathode in

ZnABs can be attributed to the rationally designed urchin-like NiCo_2S_4 microsphere architecture and the appropriate combination of urchin-like NiCo_2S_4 microsphere with S-GNS. First, the structure conversion from NiCo_2O_4 to NiCo_2S_4 via a simple sulfurization process endow the obtained NiCo_2S_4 with a drastic electrical conductivity increase, enhance mechanical and thermal stability in addition to higher electrochemical activity compared to its corresponding oxide counterparts. Second, the urchin-like NiCo_2S_4 microsphere with the unique hierarchical structure assembled from mesoporous nanoneedles can provide efficient electron/ion transportation pathways, shorten the diffusion distance of electrolyte ions, and provide high surface exposure of active sites. Third, sulfur-doping can effectively augment the catalytic activity of the composite and ultimately enhance the cycle durability of graphene by tailoring its electronic properties, manipulating its surface chemistry, and modifying its elemental composition. Additionally, the incorporation of S-GNS with urchin-like NiCo_2S_4 microsphere makes it a promising bifunctional catalyst for ORR and OER, and provides a reference to design and construct the high-performance ZnABs.

3. Conclusion

In summary, a bifunctional hybrid catalyst consisting of urchin-like NiCo_2S_4 wrapped by sulfur doped graphene nanosheet (S-GNS) has been controllably designed and prepared by hydrothermal reaction and subsequent sulfurization process. The as-prepared S-GNS/ NiCo_2S_4 catalyst exhibits excellent catalytic activity and stability for both oxygen reduction and evolution reactions, making it an exceptional bifunctional hybrid catalyst candidate for rechargeable ZnABs. Encouragingly, when employed as air-cathode in ZnABs, the S-GNS/ NiCo_2S_4 nanocomposite exhibits very low overpotential both during discharge and charge for all current densities tested, larger peak power density, and superior durability over commercial Pt/C + Ir/C mixture catalyst. The enhanced catalytic activity of the S-GNS/ NiCo_2S_4 hybrid catalyst stems from the unique merits of each component and the synergistic effect between S-GNS and NiCo_2S_4 . The urchin-like NiCo_2S_4 microsphere with the unique hierarchical structure assembled from mesoporous nanoneedles provide more catalytic active sites and efficient transport pathways for the reactant species. S-GNS not only enhance the electrocatalytic activities but also improve the conductivity and shorten the electron transfer pathway. Especially, with urchin-like NiCo_2S_4 microsphere firmly wrapped by S-GNS, the possibility of structural collapse of urchin-like NiCo_2S_4 microspheres during charge/discharge process is effectively mitigated, which is beneficial for the enhancement of the catalytic activity and durability of urchin-like NiCo_2S_4 microspheres. Additionally, the work present here may provide a new route to develop high-performance nonprecious bifunctional catalysts for ZnABs.

4. Experimental Section

Preparation of Urchin-Like NiCo_2O_4 Microsphere: All the reagents were of analytical grade and used without further purification. The synthesis processes of urchin-like NiCo_2O_4 microsphere were as follows. First,

0.29 g $\text{Ni}(\text{NO}_3)_2 \cdot 6\text{H}_2\text{O}$, 0.58 g $\text{Co}(\text{NO}_3)_2 \cdot 6\text{H}_2\text{O}$, and 0.12 g urea were added into 50 mL distilled de-ionized (DDI) water. Then, the obtained mixture was stirred at room temperature for several minutes to form a clear pink solution and transferred into an autoclave kept at 160 °C for different hydrothermal reaction time. Finally, the precipitate collected by centrifugation was dried overnight at 60 °C, and then annealed in air at 300 °C for 2 h.

Preparation of S-GNS/ NiCo_2S_4 Composites: S-GNS/ NiCo_2S_4 composites were prepared by the following procedures. First, the NiCo_2O_4 microspheres with positively charged surface were obtained by modification with aminopropyltrimethoxysilane (APS). In a typical process, 0.6 g NiCo_2O_4 microspheres were added into 50 mL isopropanol under stirring. Then, the above mixture solution after the addition of 0.3 mL APS was refluxed at 80 °C for 8 h. After drying at 60 °C overnight, the modified NiCo_2O_4 microspheres were added in 100 mL DDI water, followed by the addition of 60 mL GO suspension (0.5 mg mL⁻¹). Afterward, the result product was collected and dried at 60 °C overnight. Finally, the obtained sample was sulfurized at 300 °C for 2 h with sulfur powder as a sulfur source. For comparison, the NiCo_2S_4 sample was prepared by the same synthesis procedure but in the absence of GO. Here, the GO (Figure S12, Supporting Information) was synthesized by the modified Hummer's method.

Morphological and Structural Characterization: A field emission SEM (LEO 1350) and TEM (JEOL 2010F) were used to characterize the morphology and structure of the obtained samples. XRD (MiniFlex 600, Rigaku) was performed to investigate the phase and crystallite structure of the sample. XPS was carried out on a Thermo Scientific K-Alpha spectrometer to analyze the chemical compositions and states of the sample. Raman spectra were obtained on a Senterra Raman detection system (Bruker Optics) using a 532 nm laser.

Electrochemical Characterization: A mixture of 2 mg catalyst, 1 mg KJ-600, 500 μL iso-propanol and 30 μL Nafion solution (2.5 wt%) was ultrasonicated for 30 min to formulate the catalyst ink, which was carefully dropped on the glassy carbon electrode (0.19 625 cm²) with a catalyst loading of 0.42 mg cm⁻². The performance of the as-prepared catalysts was investigated using a standard three-electrode system and rotating disc electrode (RDE) equipment in an O₂/N₂ saturated 0.1 M KOH electrolyte and tested with a CHI (760D) electrochemical station. A graphite rod was used as the counter electrode, whereas a saturated calomel electrode (SCE) was implemented as the reference electrode, respectively. Here, ORR activity was characterized using CV and LSV techniques with a potential window ranging from 0 to -1.0 V (vs SCE) under different rotation speeds (400, 800, 1200, 1600, 2000, and 2400 rpm). The calculation of transferred electron number (n) is shown in the Supporting Information. OER activity was tested by scanning at 5 mV s⁻¹ from 0 to 1 V (vs SCE) with a 1600 rpm rotation speed for the RDE. Commercial Pt/C (28.8 wt% Pt) and Ir/C (20 wt% Ir) were employed as the ORR and OER reference materials, respectively. The potentials presented in this work were converted to the reversible hydrogen electrode (RHE) based on the equation: $E_{\text{RHE}} = E_{\text{SCE}} + 0.059\text{pH} + 0.241$. Additionally, a home-made rechargeable ZnABs was fabricated using zinc plate as anode, catalyst sprayed on the gas diffusion layer (29 BC, Ion Power) as air-cathode, and 6 M KOH solution with 0.2 M zinc acetate as electrolyte.

Supporting Information

Supporting Information is available from the Wiley Online Library or from the author.

Acknowledgements

The authors greatly appreciate the financial support from the Natural Sciences and Engineering Research Council of Canada (NSERC), the University of Waterloo, and the Waterloo Institute of Nanotechnology. This work was financially supported by the 111 Project (No. D17007).

Conflict of Interest

The authors declare no conflict of interest.

Keywords

bifunctional catalysts, rechargeable Zn–air batteries, sulfur-doped graphene, urchin-like NiCo₂S₄ microspheres

Received: November 16, 2017

Revised: December 8, 2017

Published online:

- [1] J. W. D. Ng, Y. Gorlin, T. Hatsukade, T. F. Jaramillo, *Adv. Energy Mater.* **2013**, 3, 1545.
- [2] I. Katsounaros, S. Cherevko, A. R. Zeradjanin, K. J. J. Mayrhofer, *Angew. Chem., Int. Ed.* **2014**, 53, 102.
- [3] G. Tan, R. Xu, Z. Xing, Y. Yuan, J. Lu, J. Wen, C. Liu, L. Ma, C. Zhan, Q. Liu, T. Wu, Z. Jian, R. Shahbazian-Yassar, Y. Ren, D. J. Miller, L. A. Curtiss, X. Ji, K. Amine, *Nat. Energy* **2017**, 2, 17090.
- [4] J.-J. Xu, Z.-W. Chang, Y. Wang, D.-F. Liu, Y. Zhang, X.-B. Zhang, *Adv. Mater.* **2016**, 28, 9620.
- [5] Y.-B. Yin, J.-J. Xu, Q.-C. Liu, X.-B. Zhang, *Adv. Mater.* **2016**, 28, 7494.
- [6] T. Sun, Z.-J. Li, H.-G. Wang, D. Bao, F.-L. Meng, *Angew. Chem., Int. Ed.* **2016**, 55, 10662.
- [7] S. Yuan, X.-L. Huang, D.-L. Ma, H.-G. Wang, F.-Z. Meng, X.-B. Zhang, *Adv. Mater.* **2014**, 26, 2273.
- [8] Y.-H. Zhu, Y.-B. Yin, X. Yang, T. Sun, S. Wang, Y.-S. Jiang, J.-M. Yan, X.-B. Zhang, *Angew. Chem., Int. Ed.* **2017**, 56, 7881.
- [9] J. Meng, C. Niu, X. Liu, Z. Liu, H. Chen, X. Wang, J. Wang, J. Li, W. Chen, X. Guo, L. Mai, *Nano Res.* **2016**, 9, 2445.
- [10] J.-S. Lee, G. Nam, J. Sun, S. Higashi, H.-W. Lee, S. Lee, W. Chen, Y. Cui, J. Cho, *Adv. Energy Mater.* **2016**, 6, 1601052.
- [11] D. U. Lee, B. J. Kim, Z. W. Chen, *J. Mater. Chem. A* **2013**, 14, 4754.
- [12] Y. G. Li, H. J. Dai, *Chem. Soc. Rev.* **2014**, 43, 5257.
- [13] C. Ma, N. Xue, J. Qiao, S. Jian, J. Zhang, *Int. J. Hydrogen Energy* **2016**, 41, 9211.
- [14] G. Li, X. Wang, J. Fu, J. Li, M. G. Park, Y. Zhang, G. Lui, Z. Chen, *Angew. Chem., Int. Ed.* **2016**, 55, 4977.
- [15] J.-S. Lee, S. Tai Kim, R. Cao, N.-S. Choi, M. Liu, K. T. Lee, J. Cho, *Adv. Energy Mater.* **2011**, 1, 34.
- [16] J. Masa, W. Xia, I. Sinev, A. Q. Zhao, Z. Y. Sun, S. Grutzke, P. Weide, M. Muhler, W. Schuhmann, *Angew. Chem., Int. Ed.* **2014**, 53, 8508.
- [17] K. Fominykh, P. Chernev, I. Zaharieva, J. Sicklinger, G. Stefanic, M. Döblinger, A. Müller, A. Pokharel, S. Böcklein, C. Scheu, T. Bein, *ACS Nano* **2015**, 9, 5180.
- [18] J. Yin, Y. Li, F. Lv, Q. Fan, Y. Zhao, Q. Zhang, W. Wang, F. Cheng, P. Xi, S. Guo, *ACS Nano* **2017**, 11, 2275.
- [19] L. Yu, J. F. Yang, X. W. Lou, *Angew. Chem., Int. Ed.* **2016**, 55, 13422.
- [20] H. Long, T. L. Shi, S. L. Jiang, S. Xi, R. Chen, S. Y. Liu, G. L. Liao, Z. R. Tang, *J. Mater. Chem. A* **2014**, 2, 3741.
- [21] X. Y. Yu, L. Yu, X. W. Lou, *Adv. Energy Mater.* **2016**, 6, 1501333.
- [22] X. Han, X. Wu, C. Zhong, Y. Deng, N. Zhao, W. Hu, *Nano Energy* **2017**, 31, 541.
- [23] A. R. Hesser, B. M. Benjamin, S. M. Walsh, P. Wang, S. K. Silverman, *Chem. Commun.* **2016**, 52, 9259.
- [24] J. J. Wang, Y. Q. Wang, F. F. Cao, Y. G. Guo, L. J. Wan, *J. Am. Chem. Soc.* **2010**, 132, 12218.
- [25] J. Suntivich, K. J. May, H. A. Gasteiger, J. B. Goodenough, S. H. Yang, *Science* **2011**, 334, 1383.
- [26] Z. Zhang, X. Wang, G. Cui, A. Zhang, X. Zhou, H. Xu, L. Gu, *Nanoscale* **2014**, 6, 3540.
- [27] X. Wu, S. Li, B. Wang, J. Liu, M. Yu, *Phys. Chem. Chem. Phys.* **2017**, 19, 11554.
- [28] J. H. Wu, S. Dou, A. L. Shen, X. Wang, Z. L. Ma, C. B. Ouyang, S. Y. Wang, *J. Mater. Chem. A* **2014**, 2, 20990.
- [29] X. Wu, X. Han, X. Ma, W. Zhang, Y. Deng, C. Zhong, W. Hu, *ACS Appl. Mater. Interfaces* **2017**, 9, 12574.
- [30] J. Meng, C. Niu, L. Xu, J. Li, X. Liu, X. Wang, Y. Wu, X. Xu, W. Chen, Q. Li, Z. Zhu, D. Zhao, L. Mai, *J. Am. Chem. Soc.* **2017**, 139, 8212.
- [31] J. Xiao, Y. Xia, C. Hu, J. Xi, S. Wang, *J. Mater. Chem. A* **2017**, 5, 11114.
- [32] S. Dou, L. Tao, J. Hou, S. Wang, L. Dai, *Energy Environ. Sci.* **2016**, 9, 1320.
- [33] Z. Ma, S. Dou, A. Shen, L. Tao, L. Dai, S. Wang, *Angew. Chem., Int. Ed.* **2015**, 54, 1888.
- [34] Q. F. Wang, X. F. Wang, J. Xu, X. Ouyang, X. J. Hou, D. Chen, R. M. Wang, G. Z. Shen, *Nano Energy* **2014**, 8, 44.
- [35] Y. Lei, Y. Wang, W. Yang, H. Yuan, D. Xiao, *RSC Adv.* **2015**, 5, 7575.
- [36] J. Guo, Z. Yin, X. Zang, Z. Dai, Y. Zhang, W. Huang, X. Dong, *Nano Res.* **2017**, 10, 405.
- [37] J. Li, S. Xiong, Y. Liu, Z. Ju, Y. Qian, *ACS Appl. Mater. Interfaces* **2013**, 5, 981.
- [38] Y. Xu, X. Gao, W. Chu, Q. Li, T. Li, C. Liang, Z. Lin, *J. Mater. Chem. A* **2016**, 4, 10248.
- [39] H. Chen, J. Jiang, L. Zhang, H. Wan, T. Qi, D. Xia, *Nanoscale* **2013**, 5, 8879.
- [40] M. Sun, J. Tie, G. Cheng, T. Lin, S. Peng, F. Deng, F. Ye, L. Yu, *J. Mater. Chem. A* **2015**, 3, 1730.
- [41] S. Peng, L. Li, C. Li, H. Tan, R. Cai, H. Yu, S. Mhaisalkar, M. Srinivasan, S. Ramakrishna, Q. Yan, *Chem. Commun.* **2013**, 49, 10178.
- [42] B. Y. Guan, L. Yu, X. Wang, S. Y. Song, X. W. Lou, *Adv. Mater.* **2017**, 29, 1605051.
- [43] J. Yang, M. Ma, C. Sun, Y. Zhang, W. Huang, X. Dong, *J. Mater. Chem. A* **2015**, 3, 1258.
- [44] F. Shahzad, P. Kumar, S. Yu, S. Lee, Y. H. Kim, S. M. Hong, C. M. Koo, *J. Mater. Chem. C* **2015**, 3, 9802.
- [45] H. L. Poh, P. Simek, Z. Sofer, M. Pumera, *ACS Nano* **2013**, 7, 5262.
- [46] F. Shahzad, P. Kumar, Y. H. Kim, S. M. Hong, C. M. Kool, *ACS Appl. Mater. Interfaces* **2016**, 8, 9361.
- [47] Y. Xue, Z. Zuo, Y. Li, H. Liu, Y. Li, *Small* **2017**, 13, 1700936.
- [48] M. Li, C. Liu, H. Zhao, H. An, H. Cao, Y. Zhang, Z. Fan, *Carbon* **2015**, 86, 197.
- [49] Q. Liu, J. Jin, J. Zhang, *ACS Appl. Mater. Interfaces* **2013**, 5, 5002.
- [50] Y. Huang, Y.-E. Miao, H. Lu, T. Liu, *Chem. - Eur. J.* **2015**, 21, 10100.
- [51] G. Fu, Y. Chen, Z. Cui, Y. Li, W. Zhou, S. Xin, Y. Tang, J. B. Goodenough, *Nano Lett.* **2016**, 16, 6516.
- [52] N. Xu, Y. Liu, X. Zhang, X. Li, A. Li, J. Qiao, J. Zhang, *Sci. Rep.* **2016**, 6, 33590.
- [53] G. Anandhababu, S. C. Abbas, J. Lv, K. Ding, Q. Liu, D. D. Babu, Y. Huang, J. Xie, M. Wu, Y. Wang, *Dalton Trans.* **2017**, 46, 1803.
- [54] Y. Li, M. Gong, Y. Liang, J. Feng, J. Kim, H. Wang, G. Hong, B. Zhang, H. Dai, *Nat. Commun.* **2013**, 4, 1805.
- [55] J. S. Lee, T. Lee, H. K. Song, J. Cho, B. S. Kim, *Energy Environ. Sci.* **2011**, 4, 4148.